Nanoscale Advances

ROYAL SOCIETY OF CHEMISTRY

PAPER

View Article Online
View Journal | View Issue

Cite this: *Nanoscale Adv.*, 2022, **4**, 4886

Composition-dependent photoconductivities in indium aluminium nitride nanorods grown by magnetron sputter epitaxy†

Hemanth Kumar Bangolla, [a] Ming-Deng Siao,[a] Yi-Hua Huang,[a] Ruei-San Chen, *[a] Agnė Žukauskaitė, [b] Justinas Palisaitis,[c] Per O. Å. Persson, [c] Lars Hultman,[c] Jens Birch[c] and Ching-Lien Hsiao[c]

Photoconduction (PC) properties were investigated for ternary indium aluminium nitride ($In_xAl_{1-x}N$) nanorods (NRs) with different indium compositions (x) from 0.35 to 0.68, as grown by direct-current reactive magnetron sputter epitaxy. Cross-sectional scanning transmission electron microscopy (STEM) reveals single-crystal quality of the vertically aligned $In_xAl_{1-x}N$ NRs. Single-rod photodetector devices with good ohmic contacts were fabricated using the focused-ion-beam technique (FIB), where the In-rich $In_{0.68}Al_{0.32}N$ NR exhibits an optimal photocurrent responsivity of 1400 A W^{-1} and photoconductive gain of 3300. A transition from a positive photoresponse to a negative photoresponse was observed, while increasing the In composition x from 0.35 to 0.57. The negative PC was further enhanced by increasing x to 0.68. A model based on the coexistence and competition of deep electron trap states and recombination centers was proposed to explain the interesting composition-dependent PC in these ternary III-nitride 1D nanostructures.

Received 15th July 2022
Accepted 29th September 2022

DOI: 10.1039/d2na00456a

rsc.li/nanoscale-advances

1. Introduction

Ternary group III-nitride semiconductors such as InGaN, AlGaN, and InAlN have been widely utilized in multiple optoelectronic device applications such as ultraviolet detectors, light emitting diodes (LEDs), laser diodes (LDs), transistors, and solar cells.[1–7] Among these, indium aluminium nitride (InAlN or $In_xAl_{1-x}N$) has been less explored than the other two compounds. Recently, the $In_xAl_{1-x}N$ system has attracted attention due to its tunable and broad direct band gap ranging from 0.7 eV (InN) in the infrared (IR) region to 6.2 eV (AlN) in the ultraviolet (UV) region[8,9] by changing the atomic ratio of In/Al. Hence, $In_xAl_{1-x}N$ compounds are particularly suitable for wavelength-selective optoelectronic devices such as photodetectors, LEDs, and LDs.[10]

Even though $In_xAl_{1-x}N$ compounds can offer a wide variety of applications, it remains less explored due to the difficulty in obtaining high-quality crystals. Researchers have employed metal organic chemical vapour deposition (MOCVD),[11,12] molecular beam epitaxy (MBE),[8,13] plasma assisted reactive evaporation,[10,14] and magnetron sputter epitaxy (MSE)[15–17] to obtain high quality $In_xAl_{1-x}N$ thin films. Among these methods, MSE is more popular for the preparation of $In_xAl_{1-x}N$ due to its advantages such as low cost, low substrate temperature, and large-area production.[15] Apart from these, sputtering allows a wide range of substrates such as sapphire, glass, quartz, silicon, SiC, and ZnO to deposit $In_xAl_{1-x}N$ compounds.[18–21] By utilizing MSE, the composition of $In_xAl_{1-x}N$ compounds can easily be tuned by varying the applied magnetron power of In and Al targets. The low-temperature deposition of MSE permits deposition of single-phase In-rich composition of $In_xAl_{1-x}N$, which is difficult to grow in other high process-temperature techniques.[15] Alizadeh *et al.* reported $In_xAl_{1-x}N$ films with high In content of $x = 0.90$ deposited by dual source reactive evaporation.[14] The $In_xAl_{1-x}N$ films with full composition range ($x = 0$–1) were also realized by room-temperature heteroepitaxy using MSE.[22]

Photodetectors based on one-dimensional (1D) nanostructures such as nanorods (NRs) and nanowires exhibit superior responsivity and detectivity due to their unique properties such as large surface-to-volume ratio, light scattering (between NRs), and reduced cross-section to the quantum confinement size regime. 1D nanomaterials effectively increase overall electron mobility and minimize charge transit time due to reduced carrier scattering from the 3D to quasi-1D mode.[23] The substantial surface effects also reduce recombination and enhance excess carrier collection efficiency, which leads to

[a]*Graduate Institute of Applied Science and Technology, National Taiwan University of Science and Technology, Taipei 10607, Taiwan. E-mail: rsc@mail.ntust.edu.tw*

[b]*Fraunhofer Institute for Organic Electronics, Electron Beam and Plasma Technology FEP, Dresden 01277, Germany*

[c]*Thin Film Physics Division, Department of Physics, Chemistry, and Biology (IFM), Linköping University, Linköping SE-581 83, Sweden*

† Electronic supplementary information (ESI) available. See https://doi.org/10.1039/d2na00456a

higher performance of the photodetectors using 1D materials.[24] Wang *et al.* fabricated a self-powered solar-blind photodetector based on AlGaN nanowires, which shows a high photocurrent density of 55 μA cm^{-2} and responsivity of 48.8 mA W^{-1} at an illumination wavelength of 254 nm.[25] Kang *et al.* reported an ultraviolet-C photodetector based on n-AlGaN nanoflowers that consist of a large number of self-assembled 1D nanowires.[26] A photoresponsivity of ~0.72 A W^{-1} and sensitivity of ~40% were obtained for the nanoflower detector. Wang *et al.* reported bidirectional photoconductivity behaviour in the p–n heterojunction of p-AlGaN/n-GaN nanowires.[27] The group III-nitride photodetectors with various device architectures such as multiple quantum shell nanowires (MQS NWs),[28] multi quantum well nanorod arrays (MQW NR),[29] photo electrochemical (PEC),[27] and avalanche photodiodes[30] also have been proposed.

In this work, we address the photoconductivity of $In_xAl_{1-x}N$ NRs with different In compositions grown by MSE. The crystalline and morphological properties of the NRs were studied by X-ray diffraction (XRD), field-emission scanning electron microscopy (FESEM), scanning transmission electron microscopy (STEM), and energy-dispersive X-ray spectroscopy (EDX) in STEM. Two-terminal $In_xAl_{1-x}N$ single-NR devices were fabricated using Pt electrodes prepared by focused-ion beam (FIB) deposition on an insulating SiO_2 (500 nm)/n^+-Si substrate. The photocurrent response measurements were performed under green light illumination with different powers in order to investigate photoconductivity in $In_xAl_{1-x}N$ single-NR devices. To explain the particular composition-dependent PC in $In_xAl_{1-x}N$ single-NR devices, a PC mechanism based on the coexistence of electron traps and recombination centers is proposed. To date photoconductivity (PC) studies in ternary $In_xAl_{1-x}N$ and especially its nanorods are rare. This work is the first report dealing with the systematic study of PC performance in $In_xAl_{1-x}N$ nanorods with different high-indium compositions.

2. Experimental details

The $In_xAl_{1-x}N$ NRs were grown on *c*-plane sapphire substrates by direct-current (dc) reactive MSE. A constant heating temperature of 400 °C was maintained for all samples. A base pressure of $<3 \times 10^{-9}$ Torr was maintained in the chamber using mechanical and turbo molecular pumps. More details can be found elsewhere.[22] High-purity Al target (99.999%, 75 mm diameter) and In target (99.999%, 50 mm-diameter) were used in reactive co-sputtering of ternary $In_xAl_{1-x}N$ NRs in a gas mixture of argon (Ar) and nitrogen (N_2). The partial pressures of Ar and N_2 were kept at 3 and 2 mTorr, respectively. For obtaining different compositions, the dc magnetron power of the Al target was varied between 200 and 80 W (P_{Al} = 200, 120, and 80 W). The power of the In (P_{In}) target was kept constant at 10 W. A sputtering time of 5 h was used for all the samples. Finally, the two terminal single NR devices were fabricated using platinum (Pt) metal electrodes deposited on the insulating SiO_2 (500 nm)/n^+-Si substrates. The fabricated devices were named $In_{0.35}Al_{0.65}N$ NR, $In_{0.57}Al_{0.43}N$ NR and $In_{0.68}Al_{0.32}N$ NR depending on the composition.

The crystalline structure and morphological properties of the as-grown NRs were characterized by $\theta - 2\theta$ scan XRD (Philips PW1710 Bragg–Brentano powder diffractometer) and FESEM (Zeiss Leo 1550) respectively. Atomic structure STEM imaging and EDX compositional analyses of the NRs were performed using a Linköping double Cs corrected FEI Titan³ 60–300, operated at 300 kV. Pt electrodes were deposited using the FIB (FEI Quanta 3D FEG) technique. Source dc bias *vs.* current measurements were done by using a semiconductor characterization system (Keithley 4200-SCS). A laser source of wavelength 532 nm was used as the illumination source for the photoconductive measurements. A calibrated power meter (Ophir Nova II) with a silicon photodiode head (Ophir PD300-UV) was used to measure the incident power of the laser. To minimize the error of the power density calculation, a holographic diffuser was used to broaden the laser beam size (~20 mm^2).

3. Results and discussion

Fig. 1 shows the XRD patterns of the $In_xAl_{1-x}N$ NR samples prepared with different Al magnetron powers (P_{Al}). All samples exhibit two diffraction peaks, from the nanorods, $In_xAl_{1-x}N(0002)$, and substrate, $Al_2O_3(0006)$, respectively. In the figure, the dashed line at 31.4° denotes the position of the InN(0002) peak and the dotted line at 36.0° denotes the position of the AlN(0002) peak.[22,31] The obtained peak position for all the samples is in between the InN and AlN peaks, and there is no peak related to any binary or In and Al metal phases. The above result indicates the exclusive formation of the compound $In_xAl_{1-x}N$. The $In_xAl_{1-x}N(0002)$ peaks confirm that the NRs are of hexagonal structure and were grown preferentially along their *c*-axis direction.[3,22] From the XRD patterns, it can be seen that decreasing P_{Al} leads to a decrease of the diffraction angle for the

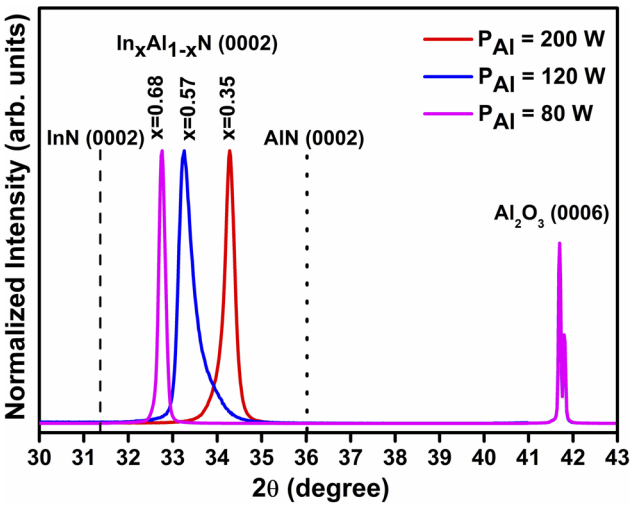

Fig. 1 XRD patterns of $In_xAl_{1-x}N$ NRs with different In contents (*x*) grown by MSE using different magnetron powers of the Al target (P_{Al}).

$In_xAl_{1-x}N$ NRs, which indicates changing $In_xAl_{1-x}N$ composition.

Assuming that all as-grown samples are stress-free, the composition of $In_xAl_{1-x}N$ NRs was estimated using Vegard's law given by[18,32]

$$c_{In_xAl_{1-x}N} = xc_{InN} + (1 - x)c_{AlN}, \quad (1)$$

where c_{InN} and c_{AlN} are the lattice constants of bulk InN and AlN and given by 5.703 Å and 4.982 Å respectively.[31] The $c_{In_xAl_{1-x}N}$ is the lattice parameter of $In_xAl_{1-x}N$ samples and it was calculated from the following equation using the $In_xAl_{1-x}N(0002)$ peak[32]

$$\frac{1}{d^2} = \frac{4}{3}\left(\frac{h^2 + hk + k^2}{a^2}\right) + \frac{l^2}{c^2}, \quad (2)$$

where d is the d-spacing, h, k, and l are the miller indices and a and c denote the lattice constants of the hexagonal system. The calculated c values of the samples grown at 200, 120, and 80 W are 5.228, 5.386, and 5.463 Å, respectively. From Vegard's law, the obtained In content x, without considering strain, is 0.35, 0.57, and 0.68, respectively. These values are in good agreement with previous reports for $In_xAl_{1-x}N$.[22,31,33] Depending on the composition, the samples were named $In_{0.35}Al_{0.65}N$, $In_{0.57}Al_{0.43}N$, and $In_{0.68}Al_{0.32}N$ for the as-grown samples at P_{Al} of 200, 120, and 80 W, respectively.

The plan-view SEM images of $In_xAl_{1-x}N$ NR samples with different compositions are depicted in Fig. 2. The different $In_xAl_{1-x}N$ NRs show similar morphology with highly dense and vertically-aligned NRs on sapphire substrates. STEM-EDX mapping was used to determine the elemental distribution and crystalline structure of the $In_{0.68}Al_{0.32}N$ NR sample as shown in Fig. 3. The cross-sectional STEM image, Fig. 3(a), shows the vertical alignment of NRs and the high-resolution STEM image, Fig. 3(b), shows a clear lattice image confirming the single-crystal quality of the NRs. The EDX elemental mapping, Fig. 3(c), reveals a uniform distribution of elements In, Al, and N across the NRs. No segregation of In-rich or Al-rich clusters is formed in the $In_xAl_{1-x}N$ NRs, and no obvious core–shell structure is observed in contrast to the $In_xAl_{1-x}N$ NRs reported by Serban *et al.*[34] An EDX line scan was employed to confirm the compositional homogeneity for the cross-sectional $In_{0.68}Al_{0.32}N$ NRs as shown in Fig. 3(d). The line scan section was performed along the yellow dashed line denoted in Fig. 3(c) in which the intensities of both In and Al signals uniformly increase and then decrease in the distance from 0 to 60 nm. The higher intensity denotes higher content of Al and In at the NR core, which is consistent with the cylindrical geometry of the rods. EDX line analysis reveals the uniform distribution of elements Al and In throughout the NR, indicating that the NRs were grown in a single-phase compound rather than a core–shell structure.[35]

It is known that the energy band gap (E_g) of $In_xAl_{1-x}N$ samples depends on the In content in the samples. Hence, it is significant for their applications in optoelectronic devices to calculate the energy band gap of $In_xAl_{1-x}N$ samples with different In contents. In accordance with the In content (x), the

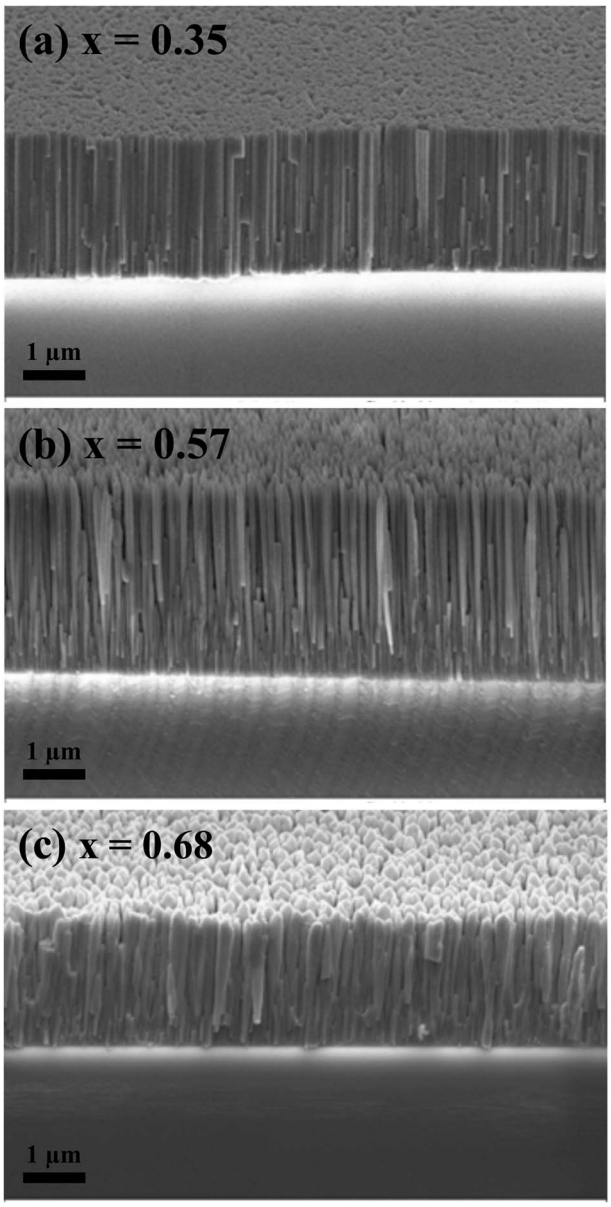

Fig. 2 Plan-view SEM images of $In_xAl_{1-x}N$ NRs with different In contents (a) $x = 0.35$, (b) $x = 0.57$, and (c) $x = 0.68$.

energy band gap (E_g) of MSE-grown $In_xAl_{1-x}N$ can be approximated by following the bowing equation[36]

$$E_{g(In_xAl_{1-x}N)} = 2.28x^2 - 4.91x + 4.17. \quad (3)$$

The calculated E_g values are 2.73, 2.11, and 1.88 eV for the samples $In_{0.35}Al_{0.65}N$, $In_{0.57}Al_{0.43}N$, and $In_{0.68}Al_{0.32}N$, respectively. It is observed that the E_g value decreases from 2.73 to 1.88 eV with increase of the In content in the samples from 0.35 to 0.68. The obtained E_g values of $In_xAl_{1-x}N$ are in close agreement with the reported values for such alloys.[14,31,37,38]

Fig. 4 shows the dark current *vs.* applied voltage (I_d–V) measurements of the two terminal single-NR devices with different compositions of $In_{0.35}Al_{0.65}N$, $In_{0.57}Al_{0.43}N$, and $In_{0.68}$

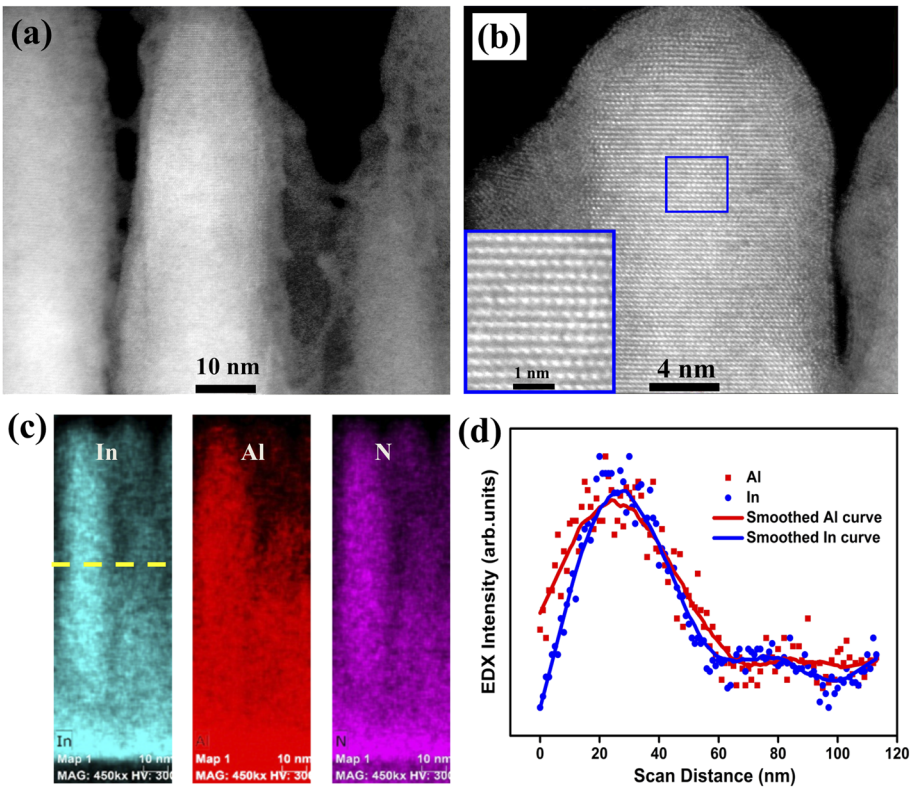

Fig. 3 (a) Cross-sectional STEM image, (b) high-resolution STEM image, inset shows a clear lattice image, (c) EDS elemental mapping of Al, In, and N, and (d) EDX line scan of $In_{0.68}Al_{0.32}N$ NRs.

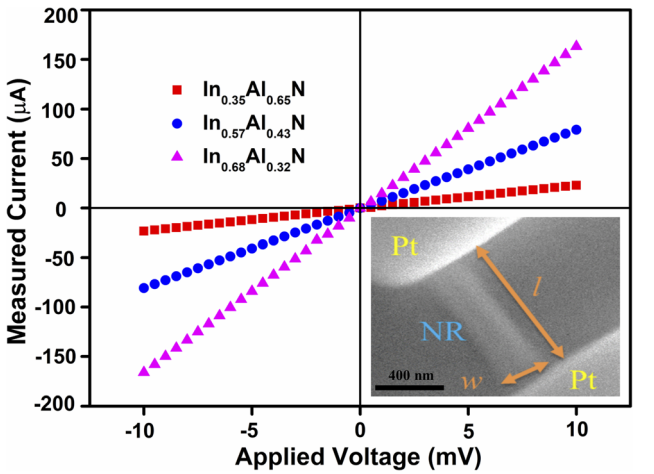

Fig. 4 I_d–V measurements of $In_xAl_{1-x}N$ single-NR devices, where the inset shows a typical SEM image of a FIB-fabricated NR device to measure the length (l) and width (w) of the conduction channel.

$Al_{0.32}N$. A typical plan-view SEM image of the NR device is shown in the inset of Fig. 4. The length and width values of the NR were obtained from the SEM image as denoted in the inset figure. For all devices, the I_d–V curves reveal linear nature, which suggests good ohmic contact between $In_xAl_{1-x}N$ NRs and Pt metal.[39,40] The I_d–V curves also show that the conductance (G) (*i.e.* slope) value increases with an increase of indium composition. The electrical conductance (G) defined as $G = I/V$ (ref. 41) can be obtained from the linear fit of the I_d–V graph. The slope of the I_d–V graph gives the conductance values 2.32×10^{-3}, 8.00×10^{-3}, and 1.64×10^{-2} Ω^{-1} for the $In_{0.35}Al_{0.65}N$, $In_{0.57}Al_{0.43}N$, and $In_{0.68}Al_{0.32}N$ devices, respectively.

The conductivity (σ) of the $In_xAl_{1-x}N$ NR devices was calculated from the following relation[41]

$$\sigma = G\frac{l}{A}, \tag{4}$$

where G is the conductance, l is the length of the conductor and A is the cross-sectional area for current flow of the conductor. The calculated conductivities of the $In_{0.35}Al_{0.65}N$, $In_{0.57}Al_{0.43}N$, and $In_{0.68}Al_{0.32}N$ NRs are 3.77×10^2, 3.25×10^3, and 6.26×10^3 Ω^{-1} cm^{-1}, respectively. The result shows that the conductivity increases with an increase of In content. In-rich ternary nitride alloys are very sensitive to formation of point and structural defects. We observed a reduction in structural quality of $In_xAl_{1-x}N$ films with the increase of In content in our previous study.[22] The increase of conductivity with the increase of In content was reported for $Al_{1-x}In_xN$ films obtained by RF sputtering.[36] Accordingly, in this work, the increase in conductivity is attributed to higher electron concentration due to generation of more donor-type defects with increase of In content.[36,42]

In Fig. 5 the typical photocurrent response of $In_xAl_{1-x}N$ NRs under green light ($\lambda = 532$ nm, $E = 2.33$ eV) illumination at a bias of 0.01 V in air is shown. For all samples, the photocurrent was recorded with different illumination powers (40 to 110

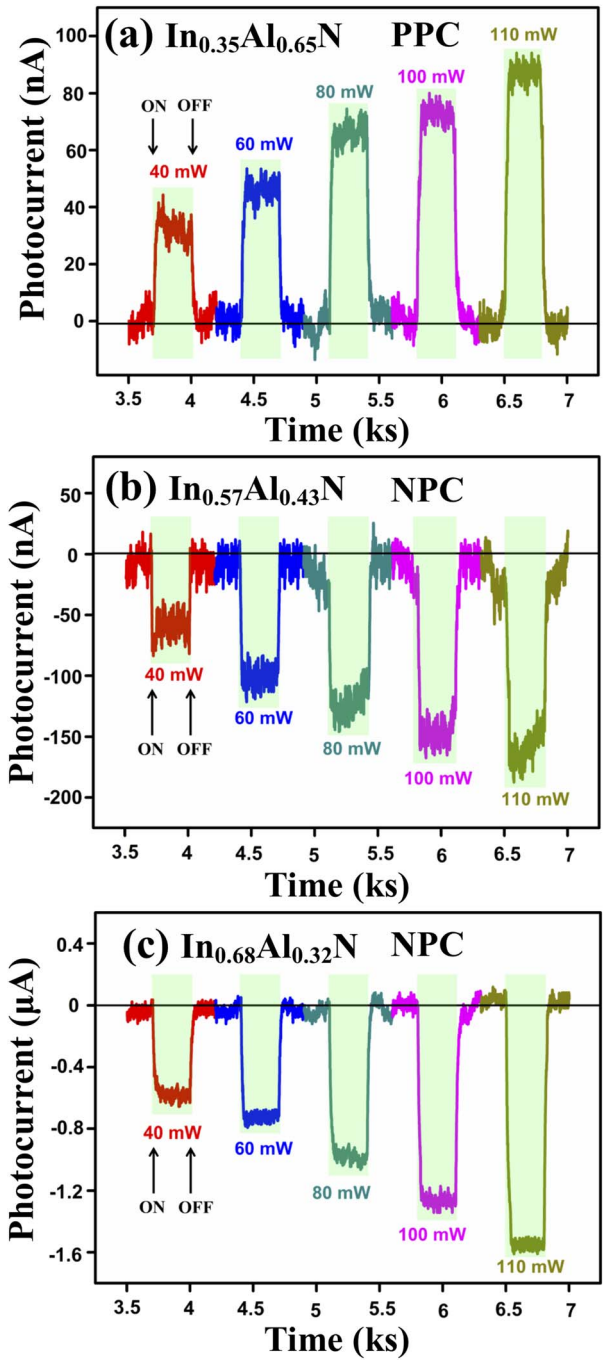

Fig. 5 Photocurrent response measurements of $In_xAl_{1-x}N$ NR devices under green light illumination with a wavelength of 532 nm and increasing laser power. ON and OFF denote the operation of the laser light source.

mW). To report photocurrent values, the background dark currents were subtracted from the response curves. The original current response curves under light illumination can be found in ESI Fig. 1.† The results reveal a clear photoresponse of the $In_xAl_{1-x}N$ NR devices to the different optical powers. All the photoresponses increase with the increase of power. It is noted that the $In_{0.35}Al_{0.65}N$ NR shows a positive photoresponse and the other two devices ($In_{0.57}Al_{0.43}N$ and $In_{0.68}Al_{0.32}N$) with higher In composition show a negative photoresponse. A clear transition from conventional positive photoconductivity (PPC) to anomalous negative photoconductivity (NPC) was observed as the In content x increases from 0.35 to 0.68.

The photocurrent *vs.* light intensity (I) curves for $In_xAl_{1-x}N$ NR devices are illustrated in Fig. 6. Optical intensity was obtained from the laser power divided by the laser spot area (diameter $\sim$ 5 mm). The photocurrent values are linearly

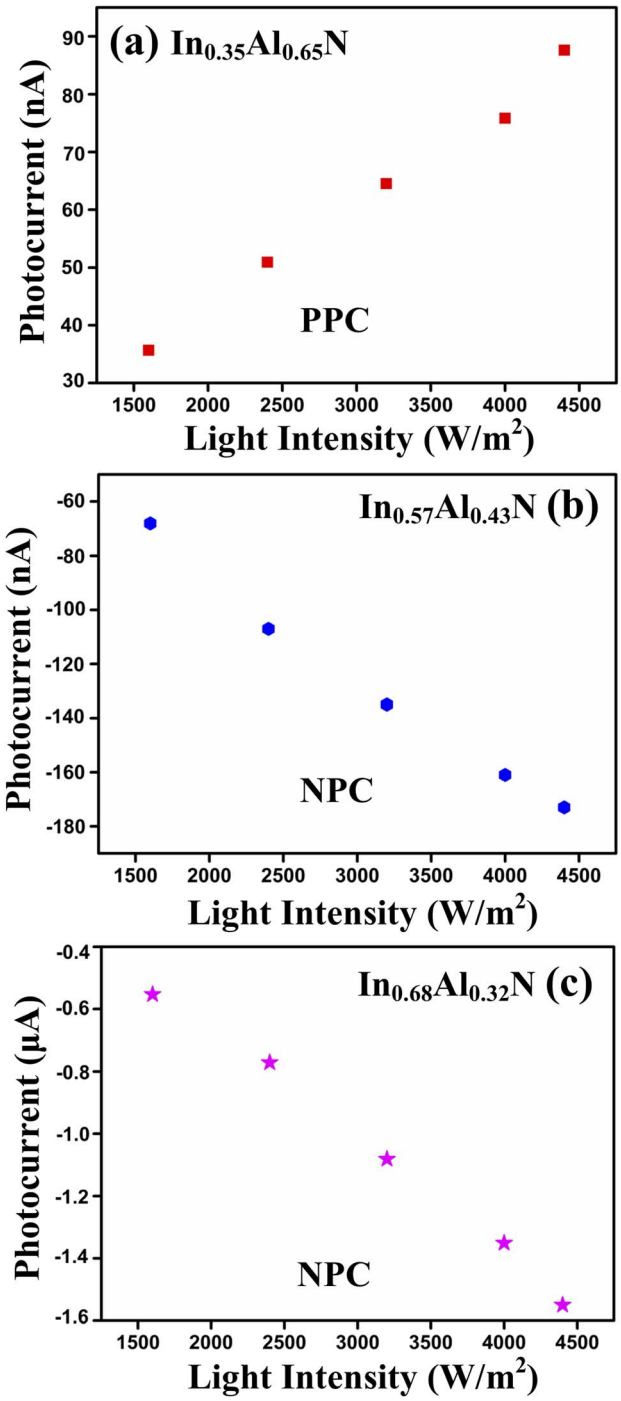

Fig. 6 Photocurrent *vs.* light intensity curves of $In_xAl_{1-x}N$ NRs with different In contents (a) $x = 0.35$, (b) $x = 0.57$, (c) $x = 0.68$.

dependent on the light intensity for the $In_{0.35}Al_{0.65}N$ NR and inversely dependent on the intensity for $In_{0.57}Al_{0.43}N$ and $In_{0.68}Al_{0.32}N$ NRs. Responsivity (R), a critical parameter determining photodetector performance, is defined as the photocurrent generated by the power of light incident on a photoconductor with an effective area (A_{PC}). R can be calculated from the formula[43]

$$R = \frac{i_p}{P} = \frac{i_p}{IA_{PC}}, \quad (5)$$

where, i_p is the photocurrent value and P is the power incident on the effective area (A_{PC}) of a photoconductor. Here, $A_{PC} = wl$ (w is the width and l is the length of the photoconductor). The calculated responsivity *vs.* light intensity curves are shown in Fig. 7(a). The results show that the R values are almost independent of the intensity (1600 to 4400 W m^{-2}). The average value of R of $In_{0.35}Al_{0.65}N$, $In_{0.57}Al_{0.43}N$, and $In_{0.68}Al_{0.32}N$ NR devices is 100, −690, and −1400 AW^{-1}, respectively. The negative sign denotes a negative photoresponse.

To investigate the physical origin of the high responsivity, photoconductive gain (Γ) was estimated. Γ is a dimensionless parameter and conceptually denotes the number of excess carriers circulating through a photoconductor per unit time before recombination. Therefore, gain is defined as the ratio of carrier lifetime (τ) to transit time (τ_t) between two electrodes and is written as[44,45]

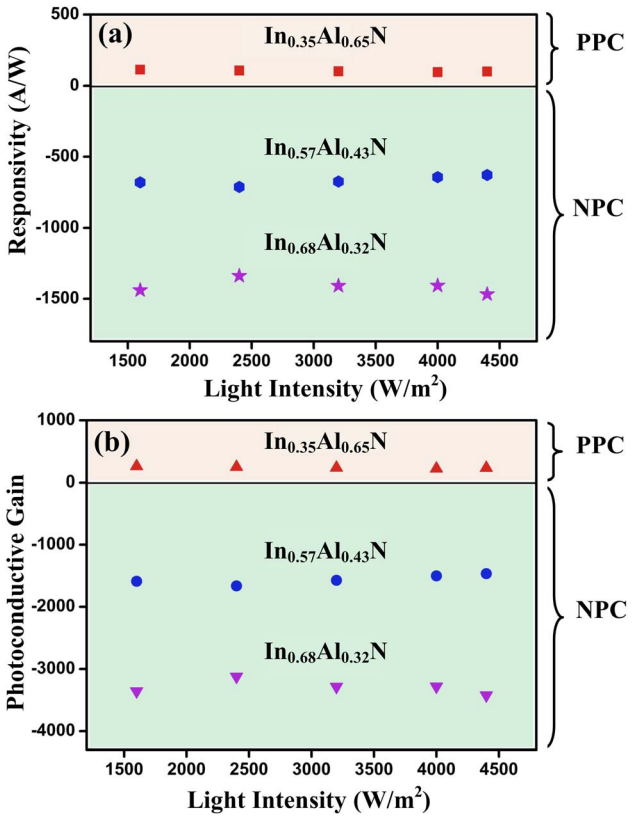

Fig. 7 (a) Responsivity and (b) photoconductive gain *vs.* light intensity of $In_xAl_{1-x}N$ NRs with different compositions.

$$\Gamma = \frac{\tau}{\tau_t}, \quad (6)$$

where $\tau_t = l/v$, here, l is the length between two electrodes and v is the drift velocity which is given by the product of mobility (μ) and applied electric field (F) *i.e.* $v = \mu F$. F can be defined as the ratio of V/l.[46] Hence, eqn (6) is modified as follows[47]

$$\Gamma = \frac{(V \times \tau\mu)}{l^2} \quad (7)$$

Γ is also defined as the number of electrons detected per absorbed photon and it is linearly proportional to responsivity and photocurrent, hence the Γ value can be estimated according to the equation[48]

$$\Gamma = \frac{E}{e}\frac{R}{\eta} = \frac{E}{e}\frac{i_p}{\eta P}, \quad (8)$$

where E is the photon energy, e is the elementary charge, and η is the quantum efficiency. To simplify the calculation, η was assumed to be unity (100%).[46,48] It is noteworthy to mention that the Γ values obtained from eqn (7) are underestimated due to the assumption of η to be unity *i.e.*, the reflected light and transmitted light through the NR are neglected.

The calculated gain *vs.* intensity curves of the $In_xAl_{1-x}N$ NRs are shown in Fig. 7(b). The results show that photoconductive gain (Γ) values are almost constant at different intensities (1600 to 4400 W m^{-2}). The average values of Γ of $In_{0.35}Al_{0.65}N$, $In_{0.57}Al_{0.43}N$, and $In_{0.68}Al_{0.32}N$ NRs are 240, −1560, and −3300, respectively. The obtained best responsivity value of the NPC device is compared with those of other NPC devices as listed in Table 1. From the table, it is clear that obtained responsivity of the $In_{0.68}Al_{0.32}N$ NR device is higher than many of the reported values for other NPC photodetectors.

To explain the transition of PPC to NPC in $In_xAl_{1-x}N$ NRs, the PC mechanism is demonstrated and proposed for the first time as follows. Generally, band-to-band (or super-bandgap) excitation generates electron–hole pairs (EHPs) as the excess carriers that results in a positive photocurrent. Since the presently used excitation energy (2.33 eV) is lower than the bandgap of the $In_{0.35}Al_{0.65}N$ NR (2.73 eV), the sub-band gap excitation is insufficient for the electrons to be excited from the valence band (VB) to the conduction band (CB) directly. They may, however, follow a two-step process as shown in Fig. 8(a). Electrons are excited from the valence band to the defect bands (such as the electron trap (ET) states) and subsequently to the conduction

Table 1 Comparison of photodetector performance of the present and reference materials with a negative photoresponse

S. No.	Material	Responsivity (A W^{-1})	Wavelength (nm)	References
1	WS_2/Au NPs	0.039	532	49
2	$Cr_2Ge_2Te_6$	340	635	50
3	rGO/AuNPs	10.05	532	51
4	rGO/WS_2	6	808	52
5	$In_{0.68}Al_{0.32}N$ NR	1400	532	Present work

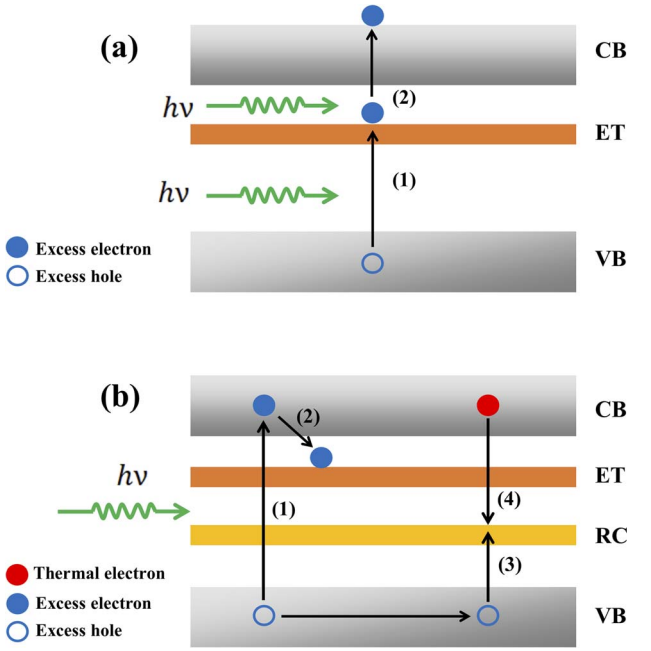

Fig. 8 Schematic band diagrams showing transitions involving the (a) PPC mechanism for $In_{0.35}Al_{0.65}N$ NRs and (b) NPC mechanism for $In_{0.57}Al_{0.43}N$ and $In_{0.68}Al_{0.32}N$ NRs. CB denotes the conduction band. VB denotes the valence band. ET denotes electron trap states. RC denotes recombination centers.

band (Step 1 and 2 in Fig. 8(a)). The sub-bandgap illumination generates excess EHPs and a positive photocurrent.

Deep electron trap states have been frequently observed in the InAlN films grown by metal–organic chemical vapour deposition.[53–55] On increasing the In content from 0.35 to 0.68, it is inferred that more In incorporation could increase the relevant defect density and at the same time could create other imperfection states such as recombination centers (RC) that sometimes originate from the deep acceptor states. The RC or deep acceptors created by high In composition have been previously reported for InAlN films.[56,57] Coexistence of the ET and RC could be responsible for the negative photoresponse. The proposed band diagram for the NPC mechanism is shown in Fig. 8(b). In this case, the In-rich $In_{0.57}Al_{0.43}N$ and $In_{0.68}Al_{0.32}N$ NRs have the bandgap ($\leq$2.11 eV) lower than the excitation energy (2.33 eV). The excited electrons could be captured by the ET *via* the super-bandgap excitation (Steps 1 and 2 in Fig. 8(b)). Subsequently if the unpaired excess holes are also captured by the RC, the positively charged RC will attract thermal electrons (Step 3 and 4 in Fig. 8(b)). Trapping of the thermal electrons lowers the carrier concentration and thus results in a negative photocurrent. This statement explains the transition from PPC to NPC in $In_xAl_{1-x}N$ NRs with increasing In composition.

4. Conclusions

Photoconductivity in $In_xAl_{1-x}N$ NRs grown by the MSE technique was investigated. The formation of $In_xAl_{1-x}N$ NRs was confirmed using XRD, plan-view FESEM, and cross-sectional STEM-EDX techniques. A clear transition from PPC to NPC has been observed in the single-crystalline $In_xAl_{1-x}N$ NRs with increasing In content. A model based on the presence of electron trap states and recombination centers is proposed to explain the noted composition-dependent photoconductivity spanning from positive to negative values. The controllable PC characteristics by the MSE process together with the high responsivity and PC gain in the $In_xAl_{1-x}N$ NRs demonstrate the potential of ternary nitride 1D nanomaterials for high-performance broad-band photodetectors.

Author contributions

Hemanth Kumar Bangolla: methodology, formal analysis, writing/original draft preparation. Ming-Deng Siao: methodology. Yi-Hua Huang: methodology. Ruei-San Chen: supervision, conceptualization, resources, writing/review & editing. Agnė Žukauskaitė: investigation. Justinas Palisaitis: investigation. Per O. Å. Persson: investigation. Lars Hultman: investigation. Jens Birch: investigation. Ching-Lien Hsiao: investigation. All authors discussed the results and approved the final version of the manuscript.

Conflicts of interest

The authors declare that there are no conflicts of interest to disclose.

Note added after first publication

This article replaces the version published on the 30th of September, which contained an error in eqn (7).

Acknowledgements

Author R. S. C. acknowledges the support of the Ministry of Science and Technology. (MOST) of Taiwan (Grant No. MOST 108-2628-M-011-001-MY3, MOST 109-2622-E-011-034, and MOST 110-2622-E-011-017). Author C.-L. H. acknowledges the support of the Swedish Research Council (Grant No. 2018-04198), Swedish Energy Agency (Grant No. 46658-1), and STINT Foundation (Grant No. MG2019-8485). The Swedish Government Strategic Research Area in Materials Science on Functional Materials at Linköping University (Faculty Grant SFO-Mat-LiU 2009-00971) is acknowledged for financial support. The Knut and Alice Wallenberg Foundation is acknowledged for support of the electron microscopy laboratory in Linköping and for project funding (KAW 2020.0033). The Swedish Research Council and the Swedish Foundation for Strategic Research are acknowledged for access to ARTEMI, the Swedish National Infrastructure in Advanced Electron Microscopy (Grant No. 2021-00171 and RIF21-0026).

References

1 R. B. Chung, F. Wu, R. Shivaraman, S. Keller, S. P. Denbaars, J. S. Speck and S. Nakamura, *J. Cryst. Growth*, 2011, **324**, 163–167.

2 F. Wang, S. F. Li, Q. Sun and Y. Jia, *Solid State Sci.*, 2010, **12**, 1641–1644.
3 R. S. Chen, C. C. Tang, C. L. Hsiao, P. O. Holtz and J. Birch, *Appl. Surf. Sci.*, 2013, **285**, 625–628.
4 H. Yu, M. H. Memon, D. Wang, Z. Ren, H. Zhang, C. Huang, M. Tian, H. Sun and S. Long, *Opt. Lett.*, 2021, **46**, 3271–3274.
5 S. Ali and M. Usman, *Eur. Phys. J. Plus*, 2022, **137**, 1–7.
6 H. Zhang, F. Liang, K. Song, C. Xing, D. Wang, H. Yu, C. Huang, Y. Sun, L. Yang, X. Zhao, H. Sun and S. Long, *Appl. Phys. Lett.*, 2021, **118**, 242105.
7 P. Nath, A. Biswas and V. Nath, *Microsyst. Technol.*, 2021, **27**, 301–306.
8 W. C. Chen, Y. H. Wu, C. Y. Peng, C. N. Hsiao and L. Chang, *Nanoscale Res. Lett.*, 2014, **9**, 1–7.
9 R. C. Cramer, E. C. H. Kyle and J. S. Speck, *J. Appl. Phys.*, 2019, **126**, 035703.
10 J. Chen, L. Shen, D. Qi, L. Wu, X. Li, J. Song and X. Zhang, *Ceram. Int.*, 2022, **48**, 2802–2810.
11 H. Kim-Chauveau, P. DeMierry, J. M. Chauveau and J. Y. Duboz, *J. Cryst. Growth*, 2011, **316**, 30–36.
12 N. Hatui, M. Frentrup, A. A. Rahman, A. Kadir, S. Subramanian, M. Kneiss and A. Bhattacharya, *J. Cryst. Growth*, 2015, **411**, 106–109.
13 Y. H. Wu, Y. Y. Wong, W. C. Chen, D. S. Tsai, C. Y. Peng, J. S. Tian, L. Chang and E. Y. Chang, *Mater. Res. Express*, 2014, **1**, 015904.
14 M. Alizadeh, V. Ganesh, H. Mehdipour, N. F. F. Nazarudin, B. T. Goh, A. Shuhaimi and S. A. Rahman, *J. Alloys Compd.*, 2015, **632**, 741–747.
15 W. Lv, L. Shen, J. Liu, J. Chen, L. Wu, D. Qi, G. Zhang and X. Li, *Appl. Surf. Sci.*, 2020, **504**, 144335.
16 H. F. Liu, C. G. Li, K. K. Ansah Antwi, S. J. Chua and D. Z. Chi, *Mater. Lett.*, 2014, **128**, 344–348.
17 J. Palisaitis, C. L. Hsiao, L. Hultman, J. Birch and P. O. Å. Persson, *Acta Mater.*, 2013, **61**, 4683–4688.
18 C. J. Dong, M. Xu, Q. Y. Chen, F. S. Liu, H. P. Zhou, Y. Wei and H. X. Ji, *J. Alloys Compd.*, 2009, **479**, 812–815.
19 T. Peng, J. Piprek, G. Qiu, J. O. Olowolafe, K. M. Unruh, C. P. Swann and E. F. Schubert, *Appl. Phys. Lett.*, 1997, **71**, 2439–2441.
20 K. Sato, J. Ohta, S. Inoue, A. Kobayashi and H. Fujioka, *Appl. Phys. Express*, 2009, **2**, 0110031–0110033.
21 K. Ueno, A. Kobayashi, J. Ohta, H. Fujioka, H. Amanai, S. Nagao and H. Horie, *Phys. Status Solidi RRL*, 2009, **3**, 58–60.
22 C. L. Hsiao, J. Palisaitis, M. Junaid, P. O. Å. Persson, J. Jensen, Q. X. Zhao, L. Hultman, L. C. Chen, K. H. Chen and J. Birch, *Thin Solid Films*, 2012, **524**, 113–120.
23 N. A. A. Zulkifli, K. Park, J. W. Min, B. S. Ooi, R. Zakaria, J. Kim and C. L. Tan, *Appl. Phys. Lett.*, 2020, **117**, 191103.
24 S. Ju, K. Lee, M. H. Yoon, A. Facchetti, T. J. Marks and D. B. Janes, *Nanotechnology*, 2007, **18**, 155201.
25 D. Wang, C. Huang, X. Liu, H. Zhang, H. Yu, S. Fang, B. S. Ooi, Z. Mi, J. H. He and H. Sun, *Adv. Opt. Mater.*, 2021, **9**, 1–8.
26 S. Kang, R. Nandi, H. Kim, K. U. Jeong and C. R. Lee, *J. Mater. Chem. C*, 2018, **6**, 1176–1186.
27 D. Wang, X. Liu, Y. Kang, X. Wang, Y. Wu, S. Fang, H. Yu, M. H. Memon, H. Zhang, W. Hu, Z. Mi, L. Fu, H. Sun and S. Long, *Nat. Electron.*, 2021, **4**, 645–652.
28 W. Lu, N. Nakayama, K. Ito, S. Katsuro, N. Sone, Y. Miyamoto, K. Okuno, M. Iwaya, T. Takeuchi, S. Kamiyama and I. Akasaki, *ACS Appl. Mater. Interfaces*, 2021, **13**, 54486–54496.
29 A. Fan, Z. Zhuang, X. Zhang, C. Li, H. Jiang, S. Chen, X. Luo, G. Hu and Y. Cui, *J. Alloys Compd.*, 2021, **885**, 161166.
30 D. Ji, B. Ercan, G. Benson, A. K. M. Newaz and S. Chowdhury, *Appl. Phys. Lett.*, 2020, **116**, 211102.
31 A. Núñez-Cascajero, S. Valdueza-Felip, L. Monteagudo-Lerma, E. Monroy, E. Taylor-Shaw, R. W. Martin, M. González-Herráez and F. B. Naranjo, *J. Phys. D: Appl. Phys.*, 2017, **50**, 065101.
32 N. Afzal, M. Devarajan and K. Ibrahim, *J. Alloys Compd.*, 2015, **652**, 407–414.
33 Z. Dridi, B. Bouhafs and P. Ruterana, *Semicond. Sci. Technol.*, 2003, **18**, 850–856.
34 E. A. Serban, P. O. Å. Persson, I. Poenaru, M. Junaid, L. Hultman, J. Birch and C. L. Hsiao, *Nanotechnology*, 2015, **26**, 215602.
35 C. L. Hsiao, J. Palisaitis, M. Junaid, R. S. Chen, P. O. Å. Persson, P. Sandstrom, P. O. Holtz, L. Hultman and J. Birch, *Appl. Phys. Express*, 2011, **4**, 115002.
36 J. J. Chen, D. L. Qi, X. F. Li, J. Y. Song and L. H. Shen, *Appl. Phys. A: Mater. Sci. Process.*, 2022, **128**, 1–8.
37 W. Song, T. Li, L. Zhang, W. Zhu and L. Wang, *J. Alloys Compd.*, 2021, **885**, 160977.
38 M. Alizadeh, V. Ganesh, A. Pandikumar, B. T. Goh, S. Azianty, N. M. Huang and S. A. Rahman, *J. Alloys Compd.*, 2016, **670**, 229–238.
39 M. D. Siao, W. C. Shen, R. S. Chen, Z. W. Chang, M. C. Shih, Y. P. Chiu and C. M. Cheng, *Nat. Commun.*, 2018, **9**, 1442.
40 H. W. Yang, H. F. Hsieh, R. S. Chen, C. H. Ho, K. Y. Lee and L. C. Chao, *ACS Appl. Mater. Interfaces*, 2018, **10**, 5740–5749.
41 Y. H. Huang, R. S. Chen, J. R. Zhang and Y. S. Huang, *Nanoscale*, 2015, **7**, 18964–18970.
42 S. Surender, S. Pradeep, K. Prabakaran, S. M. Sumithra, S. Singh and K. Baskar, *J. Alloys Compd.*, 2018, **734**, 48–54.
43 M. Anandan, H. F. Hsieh, F. C. Liu, C. Y. Chen, K. Y. Lee, L. C. Chao, C. H. Ho and R. S. Chen, *Nanotechnology*, 2020, **31**, 465201.
44 P. Bhattacharya, *Semiconductor Optoelectronic Devices*, Prentice-Hall Inc., New Jersey, 1997, Chap. 8, pp. 346–348.
45 M. Razeghi and A. Rogalski, *J. Appl. Phys.*, 1996, **79**, 7433–7473.
46 R. S. Chen, H. Y. Tsai, Y. S. Huang, Y. T. Chen, L. C. Chen and K. H. Chen, *Appl. Phys. Lett.*, 2012, **101**, 113109.
47 R. S. Chen, C. A. Chen, H. Y. Tsai, W. C. Wang and Y. S. Huang, *J. Phys. Chem. C*, 2012, **116**, 4267–4272.
48 F. González-Posada, R. Songmuang, M. Den Hertog and E. Monroy, *Nano Lett.*, 2012, **12**, 172–176.
49 B. H. Kim, S. H. Kwon, H. H. Gu and Y. J. Yoon, *Phys. E*, 2019, **106**, 45–49.
50 L. Xie, L. Guo, W. Yu, T. Kang, R. K. Zheng and K. Zhang, *Nanotechnology*, 2018, **29**, 464002, 0–7.

51 Q. Wang, Y. Tu, T. Ichii, T. Utsunomiya, H. Sugimura, L. Hao, R. Wang and X. He, *Nanoscale*, 2017, **9**, 14703–14709.
52 S. Ratha, A. J. Simbeck, D. J. Late, S. K. Nayak and C. S. Rout, *Appl. Phys. Lett.*, 2014, **105**, 243502.
53 Z. Chen, K. Fujita, J. Ichikawa, Y. Sakai and T. Egawa, *Jpn. J. Appl. Phys.*, 2011, **50**, 081001.
54 M. A. Py, L. Lugani, Y. Taniyasu, J. F. Carlin and N. Grandjean, *Phys. Rev. B: Condens. Matter Mater. Phys.*, 2014, **90**, 115208, 1–13.
55 D. Johnstone, J. H. Leach, V. A. Kovalskii, Q. Fan, J. Xie and H. Morkoç, *Gall. Nitride Mater. Devices IV*, 2009, **7216**, 72162R.
56 R. E. Jones, S. X. Li, K. M. Yu, J. W. Ager, E. E. Haller, W. Walukiewicz, H. Lu and W. J. Schaff, *J. Phys. D: Appl. Phys.*, 2009, **42**, 095406.
57 P. Chauhan, S. Hasenöhrl, E. Dobročka, L. Vančo, R. Stoklas, J. Kováč, P. Šiffalovič and J. Kuzmík, *Appl. Surf. Sci.*, 2019, **470**, 1–7.